Spatial and temporal heterogeneity in supercooled glycerol: Evidence from wide field single molecule imaging

Stephan A. Mackowiak, Tobias K. Herman,[a] and Laura J. Kaufman[b]
Department of Chemistry, Columbia University, New York, New York 10027, USA

We quantify spatial and temporal heterogeneity in supercooled glycerol at $T=T_g+14$ K employing a widefield detection scheme and using rubrene as the probe molecule. We describe how microscopy configuration affects measured intensity, linear dichroism, and the resulting autocorrelation function. Rotational relaxation times τ_c of 241 probe molecules are measured, and we find spatial heterogeneity over almost three orders of magnitude present at this temperature. An approach for detecting temporally heterogeneous molecules and quantifying exchange times is introduced. Of molecules that can be assessed, $\sim 15\%$ display evidence of temporal heterogeneity–changes of τ_c during the measurement–that are detected with the analysis technique employed. Exchanges between dynamically disparate environments occur rarely but in the proportion expected given the rarity of very slowly rotating molecules present. Heterogeneous molecules are characterized by persistence and exchange times. Median exchange and persistence times of the molecules identified as heterogeneous relative to glycerol's structural relaxation time τ_α are found to be $\tau_{ex}/\tau_\alpha=202$ and $\tau_{pers}/\tau_\alpha=405$, respectively. These results are discussed in the context of values of exchange times that have been determined in other experiments. © *2009 American Institute of Physics.*
[doi:10.1063/1.3277141]

I. INTRODUCTION

Amorphous systems lacking long range order in the temperature range between the melting temperature T_m and the glass transition temperature T_g are known as supercooled liquids. Very different chemical species including metals, small organic molecules, and polymers can exist in the supercooled state. Though such molecules exhibit very different intramolecular and intermolecular interactions, supercooled liquids of all types display striking similarities, including nonexponential relaxations. Such behavior has been attributed to spatial and/or dynamic heterogeneity.[1] We use the term spatial heterogeneity to refer to the presence of distinct regions in the supercooled liquid. Each such region may exhibit exponential relaxations but with time constants that may differ by orders of magnitude. We use the term temporal heterogeneity to refer to alterations in the dynamics of the system or a given spatial region within the system over time. The picture of the supercooled liquid as a mosaic of local environments has been used widely to describe, explain, and guide experimental and theoretical work in the area.[2]

A wide range of experimental techniques including photobleaching,[3–6] nuclear magnetic resonance (NMR),[7–11] spectral hole burning,[12,13] rheology,[14–16] dielectric spectroscopy,[17–19] and single molecule (SM) experiments[20–27] have provided evidence for the existence of heterogeneous dynamics in supercooled liquids. To straightforwardly demonstrate both spatial and temporal heterogeneity and distinguish between them, simultaneous spatial and temporal resolution is required. Of the techniques that have been used to probe supercooled liquids, only SM microscopy achieves this goal. In SM microscopy, heterogeneous dynamics can be easily identified by following dynamics of many SM probes in the same sample simultaneously or serially. Breadth of relaxation times of such probes reports on spatial heterogeneity. Changes in particular molecules' dynamics over time reveal temporal heterogeneity. While SM microscopy has straightforwardly confirmed the presence of spatial heterogeneity in supercooled liquids, agreement on the presence of and time scales associated with temporal heterogeneity is still lacking.

A recent SM study followed rotational dynamics of probe molecules in supercooled glycerol.[25] Clear evidence for spatial heterogeneity was found but environmental exchange was seen rarely enough that the authors concluded that the exchange time (τ_{ex})–the typical time over which a molecule exhibits dynamics characterized by a single time constant–was at least 10^6 times longer than the average structural relaxation time (τ_α) in glycerol in the range of $\sim 1.05-1.12T_g$. This finding stands in contrast to conclusions drawn from other subensemble (but not SM) measurements in another small organic molecule, orthoterphenyl (OTP). Here, photobleaching experiments found $\tau_{ex}/\tau_\alpha \sim 1000$ at $1.01T_g$ and $\tau_{ex}/\tau_\alpha \sim 60$ at $1.02T_g$ while multidimensional NMR experiments showed $\tau_{ex}/\tau_\alpha \sim 1$ at $1.04T_g$.[4,11,28] The differences between τ_{ex}/τ_α values and their temperature dependence in OTP and glycerol have not been explained. Difference in the fragility of OTP and glycerol may be important but differences in experimental technique and analysis, including in the definition of τ_{ex}, may play a role as well.

[a]Present address: Department of Physics, Engineering, and Geosciences, Montgomery College, Rockville, MD 20850.
[b]Author to whom correspondence should be addressed. Electronic mail: kaufman@chem.columbia.edu.

In this paper, we focus on determining the breadth of spatial and temporal heterogeneity in glycerol at 204 K ($T_g + 14$ K; $1.07 T_g$) as revealed by widefield (WF) SM microscopy using rubrene as the SM probe. WF SM microscopy allows for efficient parallel data acquisition in contrast to the serial data collection required in a confocal approach. While WF SM microscopy has been used previously to study supercooled systems,[21,26] confocal configurations are more frequently employed.[20,22–25] First, we describe how microscopy configuration affects measured intensity, linear dichroism (LD), and resulting autocorrelation functions (ACFs). We revisit how trajectory length affects the ACF and evaluate several techniques for obtaining relaxation times from short trajectories. An approach similar to that proposed by Schob et al.[21] for detecting dynamic heterogeneities and quantifying exchange time is described. Finally, examples from each of the three classes of probe molecules encountered in the measurement are discussed. These are typical molecules, slow molecules, and temporally heterogeneous molecules. Of the molecules assessed, ~15% display dynamic exchange over the time scales assessed with the measurement and analysis technique described. Analysis of these temporally heterogeneous molecules reveals a median value of $\tau_{ex}/\tau_\alpha \sim 200$ in this measurement in glycerol at $1.07 T_g$. This result is discussed in the context of values of τ_{ex}/τ_α as have been determined in other experiments.

II. EXPERIMENTAL

A. Sample preparation

A 10^{-7} M rubrene (Acros Organics) / ethanol (Sigma Aldrich, spectrophotometric grade) solution was added to glycerol (Sigma Aldrich, spectrophotometric grade, <0.1% water) to give a final concentration of approximately 10^{-9} M. Before addition of the dye solution, the glycerol was photobleached for two weeks in a bleaching setup described previously.[29] The solution was spin coated (Specialty Coating Systems, Model P6204) at 8000 rpm on a small (5×5 mm^2) piece of silicon wafer (University Wafer). Just prior to spin coating, each wafer was sonicated in acetone (Sigma Aldrich, spectrophotometric grade), rinsed with Millipore water, and heated briefly in an open flame to pyrolyze any remaining impurities. Silicon was used as a substrate because of its low background fluorescence signal and its ability to partially quench fluorophores within a few nanometers of the surface.[30] The spin-coating procedure produced a glycerol film a few hundred nanometers thick in the center of the wafer and somewhat thicker at the edges, as judged by the color of the film and the interference fringes along the edges.

The sample was placed into a microscopy cryostat (Janis Research Co. Inc., Model ST-500-LN) using vacuum grease (Apiezon N) to ensure thermal contact between sample stage and silicon wafer. The cryostat was evacuated and flushed with dry nitrogen five times at room temperature to remove water that can be absorbed during spin coating.[31] While evacuating at room temperature, the pressure was not allowed to fall below 1 Torr to prevent evaporation of glycerol. We confirmed the water content of the glycerol to be repro-ducibly ≤0.5% both when removed from the bottle and after 15 min at atmospheric conditions by viscosity measurements.[15,32] The time required for spin coating and transfer of the sample to the cryostat is typically <5 min, after which the evacuation is performed: we thus expect 0.5% water to be an upper bound on the water content of the sample at the time of the experiment. The sample is subsequently cooled to 204 K at a rate of 6 ± 1 K/min. Before data acquisition, the cryostat was further evacuated for 1–2 h at 204 K to a pressure of 0.3 mTorr using a roughing pump (Edwards, ELM-18) and a turbo pump (Pfeiffer Balzers, TPH170). Pressure was measured using a convection vacuum gauge (Kurt Lesker Co., 275807).

B. Temperature control

Sample stage temperature was measured using a 100 Ω platinum resistive temperature device (Pt RTD) calibrated against a calibrated silicon diode thermometer (Lakeshore) and mounted directly on the sample stage (Fig. 1). The temperature of the sample stage was controlled using a temperature controller (Lakeshore 331S). Sample stage temperature was stable within 50 mK of the set point, with an absolute accuracy set by the Pt RTD calibration (estimated to be better than 200 mK). Sample temperature can be somewhat higher than the sample stage temperature due to heat load from the laser. To check for the presence of and potentially correct for this effect, data were recorded at the same stage temperature at three different excitation powers. Extrapolation of average probe rotational relaxation time to zero power allows correction for heating effects. In the data sets described in this paper, no heating effects were seen, and median rotational relaxation time was independent of the excitation power. Thus, no temperature correction was required.

C. Optical setup

Data were acquired using a home-built microscope in an epifluorescence configuration (Fig. 1). A frequency doubled Nd:vanadate continuous wave laser at 532 nm was the excitation source (Coherent, Verdi V-18). 1 W of the emitted light was directed to the microscope. The beam waist was reduced by a telescope (Fig. 1, L1 and L2). The beam was then passed through an acousto-optic modulator (AOM; IntraAction Corp., modulator model AOM-40 and rf driver Me-40), which was used to modulate power. The beam diameter was adjusted with another telescope (Fig. 1, L3 and L4) to the aperture of the electro-optic modulator (EOM; Conoptics, modulator M370 and amplifier 302RM). The beam was then passed through a laser line filter (Semrock, LL01–532, F1 in Fig. 1) and a $\lambda/2$ waveplate (Karl Lambrecht, MWPQ2–12). This aligned the polarization of the incoming laser light with the crystal axis of the EOM. The EOM switched the light between s and p polarization at a frequency of 1 kHz.

The excitation beam was reflected toward the objective lens by a dichroic mirror (Semrock, FF545–650-Di01-25 $\times$ 36). Retardation by the dichroic mirror can result in elliptical polarization of the laser light at the sample unless the incoming polarization is aligned with (or perpendicular to) a
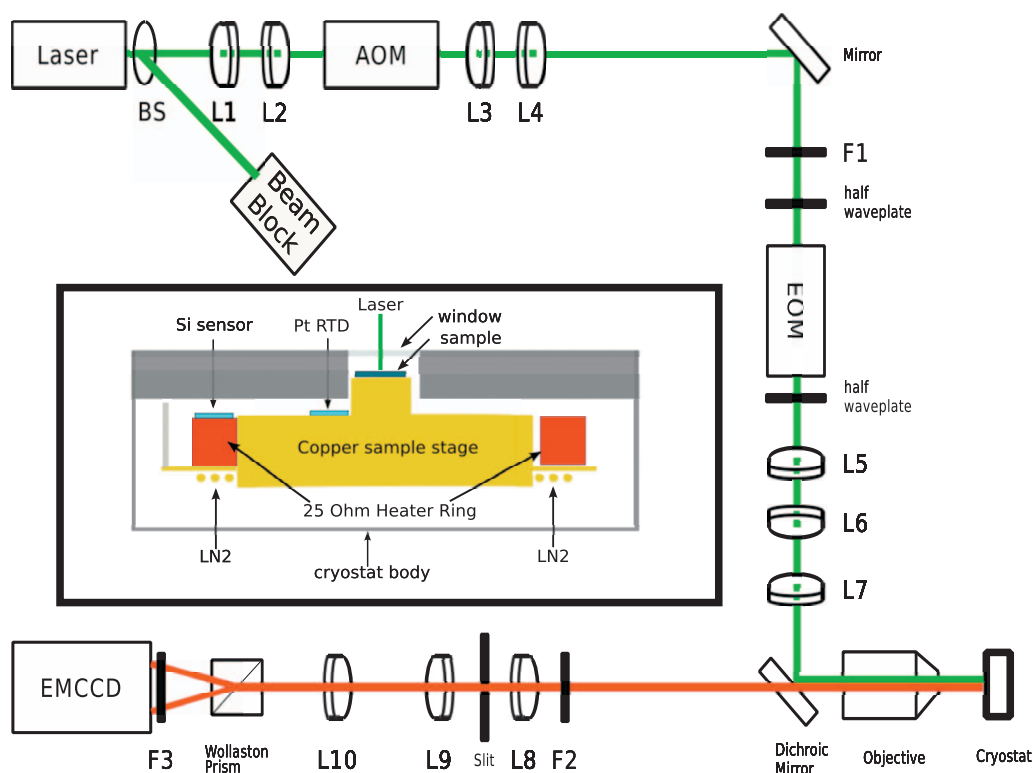
FIG. 1. Schematic diagram of home built epifluorescence SM microscope. BS=beam splitter, L=lens, F=filter, AOM=acousto-optic modulator, EOM =electro-optic modulator. Inset shows detail of the cryostat. The cryostat has two temperature sensors, but only the Pt RTD is used to determine sample temperature, as the built-in Si sensor sits atop the heating ring. The window has a thickness of 0.5 mm, and the distance between window and sample is 0.2 mm. The cryostat is cooled with liquid nitrogen (LN2). The size of the sample is 0.5×0.5 mm^2. The drawing is not to scale.

preferred axis, so a second $\lambda/2$ waveplate (Karl Lambrecht Corp., MWPAA2–12) after the EOM was used to align the incoming polarization to minimize this effect. This resulted in a polarization ratio of at least 50:1 after the objective. The telescope consisting of L5 and L6 optimized the diameter of the excitation beam and, in conjunction with the focusing lens (L7 in Fig. 1, $f=150$ mm), determined the size of the beam at the sample. L7 focused the light onto the rear focal plane of the long working distance objective with correction collar (Zeiss, LD Plan-Neofluar, air $63\times$, numerical aperture (NA)=0.75, working distance=1.5 mm), resulting in a collimated excitation beam. This objective lens allowed imaging through the 0.5-mm-thick cryostat window with an additional separation of 0.2 mm between the cryostat window and sample. For the data sets described in this paper, 15–30 mW of optical power (at a power density of $300-600$ W/cm^2) reached the sample.

The fluorescence signal was collected by the same objective in the epidirection, passed through the dichroic mirror, and further filtered by a long pass filter (Semrock, LP03–532RU-25, F2 in Fig. 1). Signal transmitted through the dichroic mirror did not experience the polarization rotation that light reflected by the dichroic did, with less than a 1% loss of polarization for linearly polarized light. A telescope (L8 and L9 in Fig. 1) with an adjustable width slit in the middle was used to crop the image before it was focused by a tube lens (L10 in Fig. 1) through a Wollaston prism (Karl Lambrecht) and another bandpass filter (Chroma, 620/160m, F3 in Fig. 1) onto an electron multiplying charge-coupled device (EMCCD) camera (Andor, iXon DV887). The Wol-

laston prism split the signal into two orthogonal polarizations, resulting in two images on the CCD chip.

A slow drift of the objective lens perpendicular to the sample plane was minimized with an autofocusing routine. This routine periodically moved the objective lens using a piezoelectric transducer (Physik Instrumente, Model P883.50) to maximize mean fluorescence intensity and skewness over the excited region to ensure the sample remained in the focal plane.

Three sets of data from two samples prepared on two days were collected as 14-bit movies at a frame rate of 5 Hz using in house LABVIEW software. The sample was continuously illuminated, and thus exposure time was 0.2 s per frame. Data were collected for 1000 s. Movies were subsequently analyzed using in-house IDL based software (ITT Visual Information Solutions).

D. Identification of molecules and extraction of intensities

Due to relatively low signal-to-noise in individual images collected, all frames in a given movie were summed prior to identification of SMs. The resulting summed movie image was filtered by convolution with a Gaussian intensity distribution. Individual molecules were then identified using the "feature" algorithm as described by Crocker and Grier.[33] Features of reasonable intensity above the background were matched up into pairs–one from the left channel and one from the right channel–by using the known separation of these channels on the CCD chip. Only molecules that were

identified in both channels were analyzed. Once matched up, each feature was checked to ensure that neighboring pixels did not contain signal from nearby fluorophores; this ensured that the signal of a given molecule was not convolved with that of another fluorophore. Fluorophores within a given distance (usually ~four pixels) of another bright feature were excluded from analysis. After exclusion of overlapping features, 279 total features remained over the three data sets analyzed. Additional factors eliminated 38 features from further analysis. These features were either of significantly different intensity than most identified features, bleached in multiple steps, blinked much more frequently than typical molecules, or had ACFs that could not be well fit. We note that in a pure glycerol sample without added probe, ~two molecules that fit criteria for further analysis can typically be identified. As such, we believe <5% of the 241 molecules analyzed could be impurities despite our rigorous attempts to exclude impurities from analysis.

Once the locations of the fluorophores were established, all further analysis was performed on the raw, unfiltered images. The intensity of the fluorophore was calculated in both channels by integrating the intensities of pixels within a given radius of the identified feature center (2.5 pixels). In order to extract true fluorophore intensities, a spatially varying background was subtracted. This background mimicked the excitation beam profile, which was somewhat inhomogeneous. As such, it was calculated for each feature individually by averaging the intensities of the pixels surrounding the feature from the limit of the integration above (2.5 pixels) out to a radius of 4.5 pixels. In order to reduce the effect of other fluorophores that sometimes border this background region, the pixels were sorted in order of intensity and the top and bottom 10% of this distribution were excluded from the average. These corrected intensities (integrated intensity minus background) were recorded for each molecule in each frame of the movie. These intensities are denoted $I_\parallel$ and $I_\perp$. LD was then constructed from each frame of the movies as

$$\text{LD} = \frac{I_\parallel - I_\perp}{I_\parallel + I_\perp}. \tag{1}$$

E. Simulation

Three-dimensional rotational diffusion of a fluorophore was simulated as a random walk along the surface of a sphere. The orientation of the transition dipole of the fluorophore is represented by a unit vector, and the rotation of this vector was calculated using quaternion rotations.[34] For each step, the rotation axis was chosen randomly. The vector was rotated about this axis by an angle whose magnitude was chosen from a Rayleigh distribution, with the diffusion constant chosen to give the desired time constant, τ_c. From these simulated trajectories, x, y, and z components of the dipole orientation were used to calculate intensity and LD as they would be detected experimentally. Simulations with a given rotational relaxation time τ_c were used to evaluate how microscopy configuration, sampling rate, and trajectory length affect ACFs of LD as will be described below.

III. RESULTS AND DISCUSSION

The objective of this work is to determine the breadth of time scales and persistence of rotational dynamics of SM probes in supercooled glycerol. These time scales are obtained from fitting ACFs of LD traces from individual probe molecules. LD is the SM analog of polarization anisotropy as measured in ensemble measurements and has therefore been widely used to probe SM orientational dynamics in supercooled liquids.[20,21,23–25,35,36] In polarization anisotropy measurements with spherical probes, nonexponentiality in the decay of the ACF is interpreted as arising from spatial and/or temporal heterogeneity.[37,38] For SM LD ACFs, such nonexponentiality cannot arise from averaging over many molecules and may thus be assumed to arise from temporal heterogeneity. However, it has been shown that nonexponentiality in the decay of LD ACFs can exist even in the presence of temporally homogeneous diffusive dynamics. Both effects from the objective lens employed and from fitting short trajectories can result in nonexponential ACFs.[23,35,39–41] Here, we address how the former effect manifests in our WF approach in comparison to the more conventional confocal approach. We then revisit how trajectory length affects exponentiality of the ACFs and describe ways to minimize effects of short trajectories on extracted relaxation timescales. A method for identifying and obtaining (multiple) rotational relaxation times and exchange times from temporally heterogeneous molecules is described. Finally, representative molecules from each of the three most common types of molecules encountered are discussed.

A. Effect of microscopy configuration on LD

Absorption and emission of photons by a fluorophore depend sensitively on the orientation of the fluorophore's transition dipole, which is defined by two angles: $0 < \theta < \pi$, the angle between the dipole and the optical axis, and $0 < \phi < 2\pi$, the angle within the sample plane. The absorption of light by fluorophores depends on their orientation with respect to the electric field of the incoming light: Abs $\propto (\vec{\mu} \cdot \vec{E})^2$ where $\vec{\mu}$ is the transition dipole of the fluorophore and $\vec{E}$ is the incident electric field. The efficiency with which emitted photons are collected also depends on the orientation of the dipole. We used linearly polarized excitation, with the incident laser switched back and forth between two orthogonal polarizations at 1 kHz, much faster than the frame rate used in this experiment. Since the total time of exposure to each polarization was equal during any single frame of the collected movies, the in-plane angular dependence of absorption disappears, leaving only a dependence of the out-of-plane angle θ.

Using collimated excitation light, as we do in our experimental configuration, the absorption probability will be proportional to the projection of the dipole into the sample plane, $\sigma_a \propto \sin^2 \theta$. For detection with a finite NA lens, detection efficiency is a function of both dipole orientation and NA of the collecting lens. When a fluorophore emits a photon, the polarization and emission direction are determined by the fluorophore's transition dipole. In the experiment described here, the emitted photons are split into orthogonal

polarizations by the Wollaston prism; in a NA ~ 0 detection geometry, one would simply have $I_\parallel \propto \sin^2 \theta \cos^2 \phi$ and $I_\perp \propto \sin^2 \theta \sin^2 \phi$. Finite NA optics affect the relative intensities of these channels, however. Following Fourkas, the intensities in two orthogonal detectors are given by

$$I_\parallel \propto A + B \sin^2 \theta + C \sin^2 \theta \cos 2\phi, \qquad (2)$$

$$I_\perp \propto A + B \sin^2 \theta - C \sin^2 \theta \cos 2\phi, \qquad (3)$$

where A, B, and C depend on the NA of the objective lens.[42] The total detected intensity is thus

$$I_{\text{tot}} = I_\parallel + I_\perp \propto A + B \sin^2 \theta \qquad (4)$$

which, as expected, depends on the out-of-plane orientation θ but not the in-plane orientation ϕ. We note that if the excitation light is focused by a high NA objective, these expressions also describe the absorption of photons by the fluorophore. Then absorption is no longer proportional to $\sin^2 \theta$ but includes additional components due to the A and C terms. If the polarization of the excitation light is isotropic, the C term disappears as the absorption will not depend on in-plane angle and

$$\text{Abs} \propto A_x + B_x \sin^2 \theta, \qquad (5)$$

where A_x and B_x refer to the NA of the excitation optics.

The total detected intensities are proportional to the product of the absorption and detection probabilities. Thus the detected intensities $I_\parallel$ and $I_\perp$ are both scaled by the excitation efficiency, which depends on θ. Thus, generally

$$I_\parallel \propto (A_x + B_x \sin^2 \theta)(A + B \sin^2 \theta + C \sin^2 \theta \cos 2\phi), \qquad (6)$$

$$I_\perp \propto (A_x + B_x \sin^2 \theta)(A + B \sin^2 \theta - C \sin^2 \theta \cos 2\phi), \qquad (7)$$

$$I_{\text{tot}} \propto (A_x + B_x \sin^2 \theta)(A + B \sin^2 \theta). \qquad (8)$$

We excite with a nearly collimated beam (i.e., NA ~ 0) and detect using the full aperture of the objective (NA $= 0.75$: $A = 0.0254$, $B = 0.0465$, and $C = 0.07111$, following Fourkas[42]). Since excitation is collimated, the total detected intensity has very strong θ dependence. Figure 2 compares total detected intensity as a function of microscopy configuration. Comparing the configuration we employ [WF excitation, NA $= 0.75$ air objective for detection (Fig. 2, red dashed line)] to focused excitation through the same objective (Fig. 2, green dotted line) shows that the WF configuration is less sensitive to out-of-plane molecules. Moreover, as expected, use of higher NA objectives [including the configuration used by Zondervan et al.[25] (Fig. 2, blue dot-dash line) and even higher NA oil objectives frequently used in SM imaging (Fig. 2, olive line)] leads to further enhanced sensitivity to molecules oriented significantly out of plane. Additional manifestations of differences in microscopy configuration both in the presence and absence of various sources of noise will be discussed below.

To analyze collected data, LD was constructed from background corrected intensities via Eq. (1). The intensities measured in each channel, and thus the LD, depend both on the orientation of the fluorophore and the NA of the detection
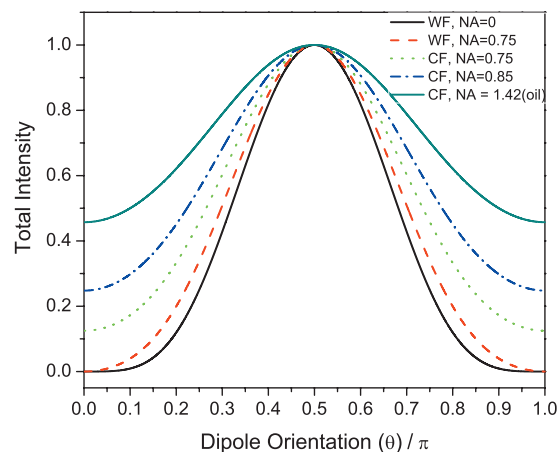

FIG. 2. Total detected intensity (from Eq. (8)) as a function of angle between optical axis and transition dipole (θ), NA, and excitation geometry. From bottom to top: the low NA limit (NA ~ 0) (black solid line), NA $= 0.75$ air objective with WF excitation (system used in this study) (red dashed line), NA $= 0.75$ and confocal excitation [green dotted line], NA $= 0.85$ air objective and confocal excitation (system used in Ref. 25) (blue dash-dot line), and NA $= 1.42$ oil objective with confocal excitation (olive solid line). Maximum intensity has been normalized.

optics. Analytically, combining Eqs. (1), (6), and (7) yields the following expression for linear dichroism:

$$\text{LD} = \frac{C \sin^2 \theta \cos 2\phi}{A + B \sin^2 \theta}. \qquad (9)$$

Before examining whether LD distributions measured experimentally match those expected from Eq. (9), it is instructive to calculate the expected LD distribution for different microscopy configurations given an isotropic array of dipole orientations. To do this in a manner consistent with experimental data (where noise may be present) requires simulations rather than an analytical approach. Thus, we compute expected LD distributions from simulation for our configuration (WF, NA $= 0.75$) and note that simulations without noise and the analytical approach represented by Eq. (9) give the same result (data not shown).

First, dipole orientations from simulations of rotational diffusion together with A, B, and C coefficients for a particular configuration are used in Eqs. (6) and (7) to retrieve $I_\parallel$ and $I_\perp$. These intensities are scaled such that the average intensity correlates to that of a typical background subtracted experimental signal. This gives a set of intensities that are used to construct the LD expected for NA $= 0.75$ independent of excitation geometry in the absence of noise. A histogram of the LD distribution expected for the configuration we employ is given by the black line in Fig. 3. Because in the absence of noise excitation geometry does not affect LD (and does not appear in the analytical result, Eq. (9)), this distribution is identical for confocal excitation through this objective (data not shown).

Once noise contributions are present in the measurement (or simulation), the analytical result given by Eq. (9) is no longer applicable. To understand how noise affects the LD distribution, noise contributions are added to the simulations and LD is calculated. First, detector noise is considered. Due to EM amplification of the CCD camera used in this study,
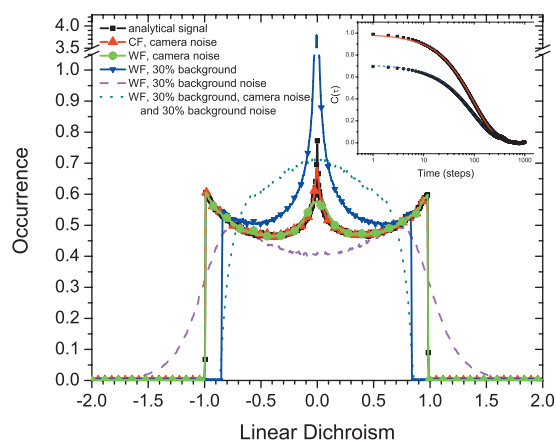
FIG. 3. LD histograms for an air objective with NA=0.75 with WF excitation, except as noted. Analytical signal (black line with squares), signal with camera noise (green line with circles), signal with camera noise for detector with confocal excitation (red line with triangles), signal with a constant background equal to 30% of the mean signal intensity (blue line with inverted triangles) as well as camera and background noise (olive dotted line), signal with camera and background noise but without constant background (purple dashed line). The purple dashed line is the raw LD distribution expected for data measured here. Lines with markers only have markers at a subset of the total points for clarity. Inset: ACF from noise free (squares) and noise-containing (circle) trajectories treated identically to experimental data with relaxation times of 100 steps fit with single exponential functions (lines). Noise-free trajectory yields $\tau_c=100.8$ steps, $R^2=0.99$. Noise-containing trajectory yields $\tau_c=98$ steps, $R^2=0.98$.

detector noise here has a variance (σ^2) two times the intensity of the signal. This variance is approximately twice that expected in the absence of the EM gain.[43] To add noise of this type to the simulations, each scaled intensity in the simulated noiseless trajectory is multiplied by a random number from a Gaussian distribution with mean equal to that intensity and variance equal to two times that intensity. The effect of detector noise is shown in Fig. 3 for a signal collected on an amplified camera with WF excitation (green line with circles) as well as with confocal excitation (red line with triangles). These results show that detector noise blunts the peak in the middle of the LD distribution. This is due predominantly to the fact that molecules that contribute to this peak are those that are oriented out of plane; these are also the molecules with the lowest detected intensities, and as such their signals are readily obscured by noise.

Noise that may emerge from subtracting the spatially varying background as described in Sec. II D is also considered. First, we note that the presence of background signal (signal that exists on the camera in the presence of pure glycerol with no added fluorescent probes) would also affect the LD distribution. Figure 3 (blue line with inverted triangles) shows the expected LD distribution in the presence of a constant background with intensity equal to 30% of the mean signal intensity. The presence of background leads to both a strong peak at zero and a contraction of the expected LD range of $-1 \leq LD \leq 1$. These are both manifestations of the fact that neither of the orthogonal intensities can be zero in the presence of background. To avoid effects of constant background, experimental signals are background subtracted as described in Sec. II D. This subtraction is imperfect, as the background is spatially varying; thus, background subtrac-

tion may introduce additional noise into the signal. Experimentally, we find that after the probe fluorophore bleaches, the standard deviation of the (background subtracted) intensity fluctuations is at maximum 30% of the mean intensity of the signal before fluorophore bleaching. Given that these fluctuations arise from several sources, 30% is considered to be an upper bound on the noise introduced by background subtraction. To assess the manifestations of such noise in the LD distribution, this additional "background noise" is added to the simulated signal. At every point in the simulated trajectory, a randomly chosen value from a Gaussian distribution centered at zero with standard deviation set to 30% of mean signal intensity [or $\sigma^2=(0.3\mu_{signal})^2$] is added to the signal. Unlike detector noise, this noise does not depend on the signal intensity at any given point.

LD distribution for a signal with both detector and background noise is shown by the purple dashed line in Fig. 3. The addition of background noise further blunts the intensity around zero and extends the range of LD beyond the expected $-1 \leq LD \leq 1$. This occurs because if signal intensity in one channel is near zero, inaccurate background subtraction (i.e., "background noise") can lead to a negative intensity in that channel. For such a signal *without* background subtraction, the LD distribution is quite different (Fig. 3, blue-green dotted line), becoming contracted and attaining a more Gaussian shape. For experimental signals measured in the WF configuration, constant background is even greater than 30% of the mean signal intensity, and background subtraction must be performed to achieve a LD histogram that is not strongly contracted. However, LD values outside the expected range that emerge from negative intensities in one channel are not meaningful and can dominate the ACF even though they only represent noise fluctuations. In order to exclude these unphysical values, in simulations and experimental LD traces, when a negative intensity is present in one channel of the background subtracted signal, that value is set to zero. This procedure eliminates values outside of the range $-1 \leq LD \leq 1$ and leads to spikes in the LD histogram at -1 and $+1$. However, as will be discussed further below, the procedure does not affect the time constant obtained from the ACF of the LD trajectory. An alternate approach using a threshold to exclude points where total intensity is less than intensity after probe photobleaching was also explored. This procedure led to LD trajectories with many gaps, and these gaps were found to affect the time constant obtained from the LD ACF (data not shown). Thus, the zeroing procedure described above is used for experimental data. We refer to LD trajectories that have not been subjected to this procedure as "raw LDs" going forward.

B. Effect of SM microscopy configuration on ACFs

We now examine whether deviations of LD from the analytically expected LD due to microscopy configuration and/or noise manifest in the ACF and resulting extracted relaxation times. As we are interested in the deviation of signal from a mean, $a(t)=LD(t)-\langle LD(t) \rangle$, where LD is the linear dichroism, we use the following definition of the autocorrelation:

$$C(t) = \frac{\sum_{t'} a(t')a(t'+t)}{\sum_{t'} a(t')a(t')}. \qquad (10)$$

Experimentally, in supercooled liquids, the rotational motion of probes may be due to rapid, uncorrelated small changes in orientation or larger less frequent angular jumps. The former case, that explored by the simulations presented, describes diffusion. Diffusion can be characterized by the correlation functions $C_l(t) = e^{-Dl(l+1)t}$ where D is the diffusion constant. Each C_l corresponds to a different set of spherical harmonics and different experimental techniques probe different correlation functions. Common techniques used to study supercooled liquids include dielectric relaxation ($l = 1$), NMR ($l=2$), and fluorescence anisotropy ($l=2$). The LD signal, however, is not composed of a single set of spherical harmonics and is not governed by any particular C_l.[44] Instead, it includes contributions from all even correlation functions. It has been shown that this can result in a LD ACF that is not well fit by an exponential (with a single associated time scale) even in the presence of homogeneous diffusive dynamics.[35,44] We assess whether this effect will significantly hinder identification of temporally heterogeneous molecules given the WF excitation configuration.

First, we follow Wei *et al.*[35] to numerically evaluate the contribution of each spherical harmonic (and associated correlation function) to the LD signal using

$$C(t) = \sum_l a_l C_l(t) \quad \text{where} \quad a_l$$

$$= \frac{1}{4\pi} \sum_m a_l \left| \int_0^{2\pi} d\phi \int_0^\pi d\theta \sin\theta \frac{C \sin^2\theta \cos 2\phi}{A + B \sin^2\theta} \right.$$

$$\left. \times Y_{l,m}(\theta,\phi) \right|^2. \qquad (11)$$

In large NA systems, $C(t)$ as probed via LD is dominated almost entirely by $C_2(t)$, leading to an almost pure exponential decay of the ACF characterized by a time constant $\tau_c = 1/(6D)$.[35,44] However, due to the dependence of total intensity on the out-of-plane angle θ (Fig. 2), signal to noise will be low when the dipole is oriented significantly out of plane, and this may influence the form of the ACF. As a first approximation to assessing the importance of this effect, the coefficients a_l are evaluated when the integration limits in Eq. (11) are adjusted to reflect the range of orientations that are probed. Assuming $\sim$30% noise, we estimate from Fig. 2 that signal from molecules outside the range of $\sim\pi/4 < \theta < 3\pi/4$ will be dominated by noise. Altering the integration limits for θ in Eq. (11) to $\pi/4$ and $3\pi/4$ leads to $a_2 = 0.95$, showing that the ACF is still dominated by the second order term and should be well fit by a single exponential in the case of homogeneous diffusion.

To more rigorously assess how microscopy configuration and noise affect the ACFs, simulated trajectories used to construct the LD histograms shown in Fig. 3 are evaluated. In these simulations, the rotational relaxation time τ_c is 100 steps. The inset of Fig. 3 shows an ACF resulting from a noise and background free simulated trajectory (of length $5000\tau_c$) for WF excitation and NA=0.75 detection. A single exponential decay fits the ACF very well, yielding $\tau_c = 100.8$ steps with $R^2 = 0.99$. Thus, employing WF excitation and a relatively low NA objective for detection does not in and of itself strongly affect either the exponentiality or the measured time constant of the ACF. Adding noise to the trajectory (as in Fig. 3, purple dashed line), results in a signal with some negative intensities analogous to the experimental signal. Adding noise and applying the zeroing procedure, i.e., setting negative intensities to zero as done for the experimental signal, lowers the initial points of the ACF but has very little effect on the time constant and goodness of fit to a single exponential. Here, the ACF yields $\tau_c = 98$ steps with $R^2 = 0.98$. We conclude that the WF configuration, even in the presence of reasonable levels of noise, background subtraction, and the zeroing procedure, does not substantially affect the exponentiality of the ACF or the value of the extracted time constant. Given these results, we expect to detect single exponential relaxations for molecules exhibiting homogeneous, diffusive rotational dynamics. While the collimated excitation geometry leads to less sensitivity to molecules oriented out of plane, this has limited manifestations in ACF evaluation, and the parallel nature of the WF approach allows collection of larger data sets than confocal methods. Since obtaining a statistically large sample set is one of the challenges of SM experiments, the WF configuration appears well suited for systematic study of dynamics in supercooled liquids.

C. Effect of trajectory length on ACFs

We have shown that the WF approach does not significantly affect exponentiality of LD ACFs of molecules exhibiting diffusive rotational motion. We now turn to another potential source of nonexponentiality in SM LD ACFs of molecules exhibiting homogeneous diffusion: short trajectories.

In the study of supercooled liquids, when ACFs are poorly fit with a single exponential they are often well fit by a stretched exponential form given by

$$C(t) = K e^{-(t/\tau_{\text{fit}})^\beta}, \qquad (12)$$

where K may deviate from unity if the autocorrelated data is noisy, and β is the stretching exponent. From such a fit, one can characterize dynamic behavior by relating τ_{fit} to rotational relaxation time τ_c via

$$\tau_c = \int_{t=0}^\infty C(t) = \frac{\tau_{\text{fit}}}{\beta} \Gamma\left(\frac{1}{\beta}\right) \qquad (13)$$

when $\beta = 1$ this reduces to a simple exponential fit and $\tau_c = \tau_{\text{fit}}$. When an ACF is best fit by a stretched exponential with $\beta < 1$, the deviation of β from 1 is typically interpreted as correlating with the breadth of heterogeneous dynamics in the probed system. For a SM trajectory, the β value indicates the degree of temporal heterogeneity demonstrated by that molecule. This interpretation, however, is not necessarily appropriate for short trajectories.[39,45] Indeed, for simulations of homogeneous diffusion of trajectory length $\sim 100\tau_c$, it was shown that the τ_c and β values obtained from stretched exponential fits spanned broadly, from $\sim$0.7 to 1.5 for normal-

ized τ_c and from 0.5 to 1.5 for β.[39,45] This illustrates that the best fit stretched exponential to a (noiseless, background free) LD ACF may have $\beta \neq 1$ even for molecules with homogeneous diffusive dynamics. As such, the deviation of the best fit value of β from 1 is not a valid measure of temporal heterogeneity in short SM trajectories. At $1000\tau_c$, the τ_c and β values were shown to be much more sharply peaked at the actual rotational relaxation time and around $\beta = 1$.[35] Unfortunately, due primarily to photobleaching, experimentally it is difficult to collect SM trajectories of $1000\tau_c$. For this reason, we revisit the most accurate way to measure relaxation time for molecules with short trajectories. Moreover, because deviation of β from 1 is not a sufficient condition for identifying temporally heterogeneous molecules, we develop a new method to detect these heterogeneities using an approach similar to that introduced in Ref. 21; this method requires evaluation of portions of the complete trajectory that are just $20\tau_c$ in length.

While stretched exponential fits may not yield accurate relaxation times for short trajectories, it has been shown that more accurate time constants can be obtained for such trajectories using a linear fit to the early portion of the ACF.[41] To confirm this, linear and stretched exponential fits for simulations as a function of trajectory length were investigated. In our implementation of the linear fit, the ACF is fit to the longer of either 20% τ_{fit} or five points. τ_c is then given by $-n/m$ where n is the y intercept and m is the slope of the fit line. Stretched exponential and linear fitting is performed on both noise free and noise-containing simulations. In addition to performing the stretched exponential and linear fits, trajectories are also analyzed with a discrete wavelet transform (DWT) method introduced by Yang[46] for detecting temporal heterogeneities. The DWT should be well suited for accurately fitting short trajectories because wavelets are localized in time and frequency.

In the experimental data presented here, frame rate is chosen to capture as many rotations as possible for typical molecules. As a result, low sampling rate trajectories with few points per rotational relaxation time are typical. High sampling rate trajectories are obtained only for molecules that rotate more slowly than the average molecule. Figure 4(a) shows results of linear, stretched exponential, and DWT fits for such high sampling trajectories as a function of trajectory length. Single exponential fits were also performed and give identical time constants as the stretched exponential fits within error (data not shown). In these simulations the relaxation time τ_c is 50 steps and there are 50 points per τ_c. For high sampling rate trajectories of length $>10\tau_c$ the linear fit overestimates the relaxation time, while the stretched exponential fit underestimates relaxation time for trajectories shorter than $30\tau_c$, observations that have been noted previously.[41] For trajectories shorter than $10\tau_c$ all methods underestimate relaxation time, with the linear fit doing so by a smaller proportion than the DWT or stretched exponential fits, which both underestimate the relaxation time by 30% at $10\tau_c$. Figure 4(b) shows results from low sampling rate trajectories, which are more typical of the experimental data collected. Here, there are ten points per τ_c rather than 50. Results from fitting trajectories of this type show that the
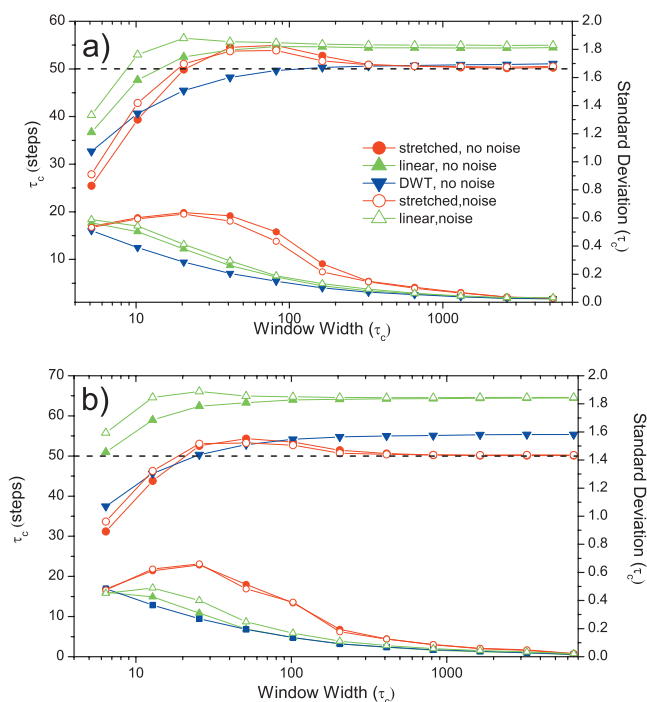

FIG. 4. Stretched exponential (red, circles), linear (green, triangles), and DWT (blue, inverted triangles) fits to simulations of homogeneous diffusive rotation as a function of window width for (a) high sampling rate (50 points per τ_c) and (b) low sampling rate (ten points per τ_c) trajectories. Left axis shows time constants and right axis shows standard deviation. Black dashed line indicates actual relaxation time of 50 steps. Filled symbols are fits from ACFs from noise-free simulated trajectories for NA=0.75 objective excitation and WF detection. Open symbols are from ACFs from simulated trajectories with camera noise, 30% background noise, background subtraction, and setting negative intensities to zero before construction of the LD.

linear fit overestimates relaxation time more significantly here (by up to 30% depending on trajectory length) than in high sampling rate trajectories. This is due to the fact that for low sampling trajectories substantial decay occurs within the portion of the ACF used for the linear fit. This overestimation persists even for very short trajectories. The stretched exponential fits report rotational relaxation time constants accurately for long trajectories, but underestimate relaxation times by ~40% for the shortest trajectories studied. While noise affects the time constant of the stretched exponential and linear fits only subtly regardless of sampling rate, DWT fits appeared strongly influenced by the presence of noise, yielding time constants significantly less than the known relaxation times of simulated trajectories (data not shown). DWT analysis was thus not used on experimental data.

Figure 4 demonstrates the importance of analyzing experimentally measured trajectories in different ways depending on details of the trajectory. Based on the results illustrated by Fig. 4, for experimental data the ACF of each molecule is first fit with a stretched exponential function, yielding $\tau_{str\,exp}$ via

$$\tau_{str\,exp} = \frac{\tau_{fit}}{\beta}\Gamma\left(\frac{1}{\beta}\right). \tag{14}$$

For all molecules with low sampling rates (<20 points per $\tau_{str\,exp}$), this fit is deemed to be the relaxation time, and $\tau_{str\,exp} = \tau_c$. For trajectories with high sampling rate, if the

trajectory is longer than $50\tau_{\text{str exp}}$, $\tau_{\text{str exp}}$ is also set as the relaxation time τ_c. For high sampling rate trajectories shorter than $50\tau_{\text{str exp}}$, where the linear fit is both more accurate and precise than the stretched exponential fit, these trajectories are refit with linear fits. For the detection of temporal heterogeneities, as will be described below, linear fits over $20\tau_c$ portions of the trajectories are used regardless of sampling rate.

D. Detecting temporally heterogeneous molecules

As described above, detection of temporally heterogeneous molecules cannot be reliably achieved by fitting a typical SM ACF to a stretched exponential and considering the deviation of β from 1. Thus, independent of the β value from the best fit stretched exponential fit, all molecules are analyzed for potential temporal heterogeneity. A method proposed by Schob et al.[21] is employed: the LD trajectory is split up into segments via a sliding window, and an ACF is calculated and fit for each segment. This results in a trajectory of rotational time constants, subsequently called τ-trajectory. A sliding window of $20\tau_c$ is selected to balance sensitivity to relatively short changes in dynamics and accuracy and precision of ACF fits. While Schob et al. used exponential fits to fit the subtrajectories,[21] based on results shown in Fig. 4, we use linear fits. This is because regardless of sampling rate, time constants derived from linear fits vary least with window width of the fitting techniques investigated. Thus, such fitting is unlikely to lead to incorrect assignment of a molecule as heterogeneous due to changes in the actual window width relative to the relaxation time of the molecule *in that window*.

After τ-trajectory is obtained, a molecule is classified as either temporally heterogeneous or homogenous. To develop criteria with which to make this judgment, data from 1000 low sampling rate and 1000 high sampling rate noise-containing simulations of molecules undergoing homogeneous diffusion were analyzed. For all simulations, τ_c for the full trajectory is determined, the sliding window autocorrelation is performed, and τ-trajectory is obtained. For simulations of low (high) sampling rate trajectories of homogeneous diffusion, 95% of the trajectories have 95% of the τ-trajectory values within 2.58 (2.41) times the median relaxation time in τ-trajectory ($\tau_{\text{traj,med}}$). This criterion thus has a false positive rate of 5%. A second criterion is based on the finding that 95% of the homogeneous trajectories have τ-trajectory distributions with standard deviations <0.68 at low sampling rate and <0.58 at high sampling rate. The second criterion is thus satisfied if the standard deviation of τ-trajectory is >0.68 or >0.58 at low or high sampling rates, respectively. We assign molecules as heterogeneous if either the first or second criteria is met. Using these criteria, 7.0% (6.5%) of low (high) sampling rate homogeneous molecules are expected to be incorrectly identified as heterogeneous. We note that both criteria are based on results of simulations. Moreover, within τ-trajectory, τ values within $20\tau_c$ of each other are not independent. Thus, these criteria are not based on or proof of any particular statistical model. Instead, the chosen criteria are empirical. While we can straightforwardly

assess the proportion of false positives using these criteria, due to the diversity of possible heterogeneous trajectories, the rate of false negatives could not be ascertained.

This approach to detecting temporal heterogeneity in the SM trajectories also gives access to time scales of dynamical exchange for those molecules deemed heterogeneous. Schob et al.[21] extracted an average time scale associated with exchange from τ-trajectory by calculating the standard deviation of the width of the relaxation time distribution for various time lags in τ-trajectory. This was then fit to the form $1-e^{-\tau/\tau_{\text{ex}}}$ with τ_{ex} the variable parameter. Both from simulations and experimental data, we find τ_{ex} determined in this manner to be strongly associated with statistical noise rather than dynamical exchange. Instead τ-trajectory of each molecule deemed heterogeneous is directly evaluated for time until the first change in dynamics and, potentially, time between dynamical exchanges. The time before the first change in dynamics is deemed the persistence time (τ_{pers}) and that between changes in dynamics is the exchange time (τ_{ex}), as described for kinetically constrained models (KCM).[47] The values and temperature dependence of persistence and exchange time need not be the same, and thus we distinguish between them.[47]

The method described to detect temporal heterogeneities is only sensitive to a subset of possible exchanges that can occur in the dynamics of a single probe molecule in a supercooled liquid. First, the approach is chiefly sensitive to typical molecules–those with relaxation times similar to the ensemble median τ_c (1.7 s)–that slow down by up to an order of magnitude for a portion of the measured trajectory. This is because the sliding window size is set by τ_c, which is calculated from a fit to the ACF over the full trajectory. If τ_c is large, the window will be large, and changes in dynamics that occur during the window will not significantly affect any point in τ-trajectory. Using smaller windows would introduce additional uncertainties due to the very low precision in determining τ_c for trajectories $<20\tau_c$ in length (Fig. 4). The choice of a window size of $20\tau_c$ sets the lower bound of exchange times we are sensitive to at $\sim10\tau_c$. Trajectory length sets the upper bound to $\sim500\tau_c$. Additionally, the window size sets a minimum trajectory length that can be assessed. All molecules with trajectories $>50\tau_c$ (τ-trajectory contains at least 31 points) are assessed for the presence of temporal heterogeneity. Of the 241 molecules analyzed for relaxation time, 195 molecules are assessed for temporal heterogeneity.

The sensitivity to temporal heterogeneity afforded by the experiment and analysis described here is different than that of subensemble experiments that have been performed previously. Indeed, both subensemble photobleaching and multidimensional NMR experiments measure the time it takes a slow subset of molecules to become average,[4,11,28] whereas the approach described here chiefly identifies average molecules that become slower. Additionally, these subensemble experiments measure the time to first change in dynamics (τ_{pers}) but term this the "exchange time" and thus $\tau_{\text{ex}}/\tau_\alpha$ as reported by those experiments is more similar to $\tau_{\text{pers}}/\tau_\alpha$ described here. We also note that the manner in which we search for the presence and timescales of temporal heteroge-
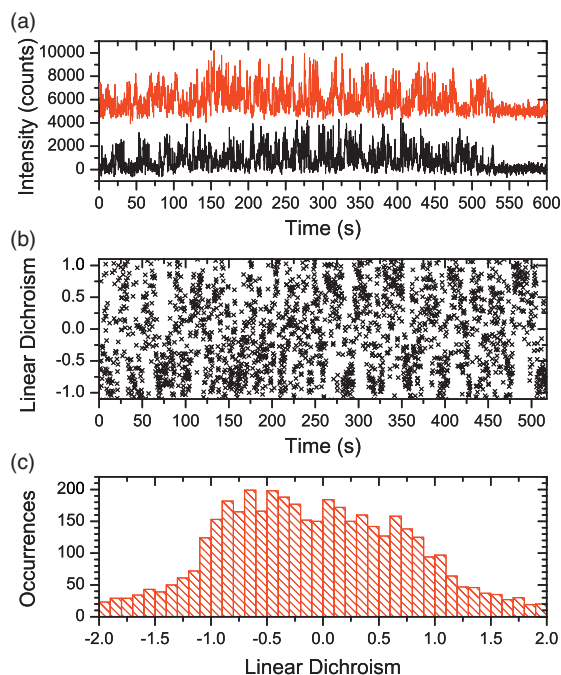
FIG. 5. Data from a representative typical molecule. (a) Background subtracted intensities in left and right-hand channels ($I_\parallel$ and $I_\perp$) with upper trace displaced vertically. (b) Raw LD calculated from background subtracted intensities in (a). Only values between -1.1 and $+1.1$ are shown. (c) Histogram of full raw LD shown in (b).
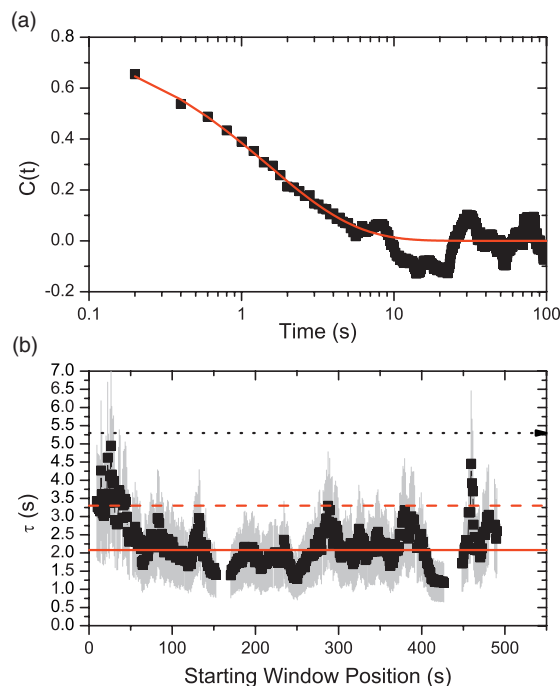

FIG. 6. (a) ACF from the typical molecule shown in Fig. 5. Stretched exponential fit with $\tau_c=1.8$ s and $\beta=0.74$ is shown by the solid line. Standard error on the points of the ACF is smaller than symbol size and therefore not shown. (b) τ-trajectory for this molecule. The error bars indicate the standard deviation of 45% associated with a low sampling rate trajectory and window width of $20\tau_c$ using linear fits as shown in Fig. 4(b), open green triangles. Solid red line is $\tau_{traj,med}=2.06$ s. Dashed red line indicates the value below which 95% of the points within τ-trajectory fall ($1.60\tau_{traj,med}=3.3$ s). Dotted black line indicates lowest position at which 95% of the points within τ-trajectory would fall for a molecule satisfying this criterion for temporal heterogeneity ($2.58\tau_{traj,med}=5.3$ s). Because the dashed red line is below the dotted black line and because the standard deviation of τ-trajectory is <0.68, this molecule is deemed homogeneous.

neity is quite different from that employed by Zondervan *et al.*[25] who look at the average relaxation times of particular molecules over long times at several temperatures.[25] The different time scales on which temporal heterogeneity is assessed in the Orrit approach compared to the approach described here limits direct comparison of τ_{ex}/τ_α from these approaches as the "exchanges" sought via each technique may not be of the same magnitude or time scale.

E. Experimental data

Having outlined the approach to data analysis we employ, we now demonstrate treatment from raw data to LD to ACF for experimental data. We then present representative examples of the three common types of molecules identified. The majority of molecules are "typical molecules," in which relaxation time is near the median relaxation time for all molecules in the data set and sampling rate is low. The second type of molecules identified is "slow molecules:" these molecules have high sampling rates and rotate significantly more slowly than the median molecule at this temperature. The final molecules described satisfy criteria for temporal heterogeneity described above and are deemed "heterogeneous molecules."

1. Typical molecules

Treatment of experimental data is demonstrated from fluorescence intensities ($I_\parallel$ and $I_\perp$) to LD, ACF, and extraction of rotational relaxation time constant in Figs. 5 and 6 for a typical rubrene molecule in glycerol at 204 K. Figure 5(a) shows intensity in two channels after background subtraction. Photobleaching is evident at ~520 s, after which noise

level can be assessed. In this case, the standard deviation of the noise is $\sim21\%$ of the mean total intensity. LD is then constructed according to Eq. (1). Raw LD [Fig. 5(b)] and a raw LD histogram [Fig. 5(c)] are shown for this molecule. The LD distribution has a shape and range very similar to that shown in Fig. 3, purple dashed line, as expected. Negative intensities present from faulty background subtraction are set to zero, and the ACF is constructed. The ACF from the LD is fit with a stretched exponential and shown in Fig. 6(a). The relaxation time, $\tau_c=1.8$ s, is obtained from the best stretched exponential fit, as the sampling rate is low ($\sim$nine points per τ_c) and the length of the trajectory is $\sim290\tau_c$.

As described in Sec. III C, regardless of the value of β for the best fit stretched exponential to the molecule's ACF (in this case $\beta=0.74$), the molecule is assessed for heterogeneity via the sliding window procedure. τ-trajectory is shown in Fig. 6(b). Here, $\tau_{traj,med}$ is 2.06 s. This value is somewhat higher than the value obtained for the stretched exponential fit over the full trajectory due to the tendency of the linear fit to overestimate relaxation time (as shown in Fig. 4). For this molecule, the standard deviation of τ-trajectory is 0.28 and 95% of the τ-trajectory values are within $1.60\tau_{traj,med}$. These values are well under the values required (0.68 and $2.58\tau_{traj,med}$) for a molecule to satisfy criteria for temporal heterogeneity. Thus, we classify this molecule as homogeneous over the length of the trajectory.
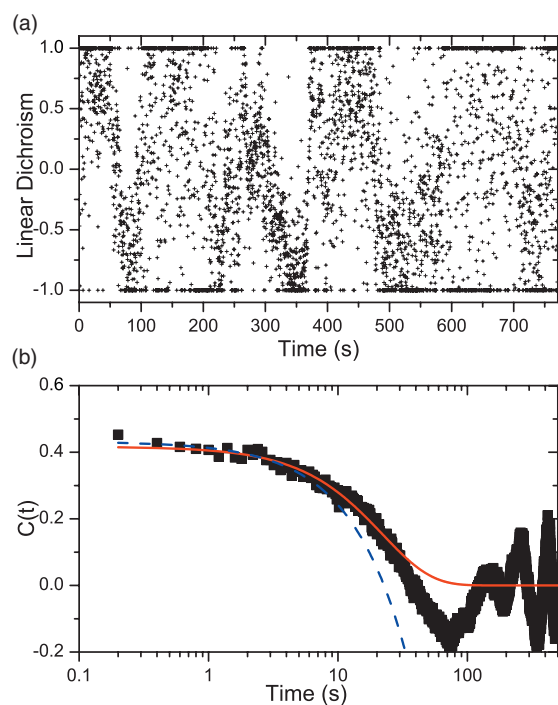
FIG. 7. (a) LD and (b) ACF from a representative slow molecule. Stretched exponential fit (red solid line) with $\tau_{\text{str exp}}=21.1$ s. Because the trajectory is at high sampling rate and shorter than $50\tau_{\text{str exp}}$, a linear fit (blue dashed line) is then applied and gives $\tau_c=22.7$ s. Standard error on the points of the ACF is smaller than symbol size and therefore not shown.

In the data set presented here in glycerol at T_g+14 K, 177 of 241 molecules are typical molecules, with low sampling rates. Indeed, the definition used for typical molecules is that their trajectories have fewer than 20 points per τ_c and thus $\tau_c<4.0$ s (or 2.35 times the median relaxation time in the data sets, 1.7 s). All but one of these 177 molecules have trajectories longer than $50\tau_c$ and are therefore subjected to the test for heterogeneity. Of the 176 typical, assessible molecules, 149 are deemed homogeneous by the criteria for temporal heterogeneity in low sampling rate trajectories described above.

2. Slow molecules

Figure 7 shows the LD and corresponding ACF of a representative slowly rotating molecule. Here, a stretched exponential fit of the ACF gives a value of 21.1 s ($\tau_{\text{str exp}}$), there is a high sampling rate (~100 points per $\tau_{\text{str exp}}$), and the length of the trajectory is $\sim30\tau_{\text{str exp}}$. Therefore, for reasons outlined in Sec. III C, the ACF is refit with a linear fit. The resulting time constant is 22.7 s, and this is taken as the relaxation time τ_c of this molecule. This molecule is not assessed for temporal heterogeneity because its trajectory is shorter than $50\tau_c$. Of the 241 molecules in the data sets described here, 65 molecules are slow, with sampling rates greater than 20 points per τ_c and relaxation times greater than 4.0 s. 39 of these have trajectories shorter than $50\tau_c$ and are not assessed for heterogeneity. Twenty one have trajectories longer than $50\tau_c$, and of these molecules, 17 are deemed homogeneous.

Because many molecules that rotate significantly more slowly than the median relaxation time of the data set pho-

tobleach before the trajectories reach $50\tau_c$, it is molecules in this category that most starkly demonstrate the importance of performing trajectory-dependent fitting to accurately report the breadth of spatial heterogeneity accessed by a SM experiment. Treating all of the molecules in the data set as described (with either stretched exponential or linear fits) leads to a median τ_c of 1.7 s and mean τ_c of 6.9 s with a spread of nearly three orders of magnitude from 0.5 to 258.7 s for rubrene in glycerol at 204 K. Fitting all of the molecules with best fit stretched exponentials results in median and mean relaxation times of 1.7 and 7.6 s, respectively. There is also a slight contraction of the range of time constants measured (0.5–162.9 s). More starkly, if one does not include molecules with trajectories shorter than $50\tau_c$ because of potential uncertainty in relaxation times determined from such short trajectories, the median and mean relaxation times of the data are 1.4 and 2.7 s, respectively, and the apparent breadth of spatial heterogeneity decreases substantially to less than two orders of magnitude (0.6–22.3 s). These differences highlight how the approach to fitting SM data can effect unintentional subensemble selection. We note that even with careful attention to including slow molecules in the assessed data, several molecules in the data set rotate too slowly for their ACFs to be fit with either stretched exponential or linear fits. Of the 38 features excluded from analysis as described in Sec. II D, three molecules are excluded because their ACFs decay too slowly to be fit.

3. Heterogeneous molecules

Figure 8 shows the LD and the corresponding ACF of a molecule identified as temporally heterogeneous. A stretched exponential fit to the ACF shown in Fig. 8(b) yields $\tau_{\text{str exp}}$ $=4.4$ s (with $\beta=0.44$). The trajectory is $\sim100\tau_{\text{str exp}}$, τ_c $=4.4$ s, and the trajectory is that of a "slow molecule" as described above. This molecule, however, proves to be temporally heterogeneous according to the criteria described. Figure 8(c) shows the result of the sliding window analysis. Here, 95% of the points in τ-trajectory are found within $3.4\tau_{\text{traj,med}}$ and the standard deviation of τ-trajectory is 0.72. Both values are well outside the range expected for homogeneous rotational diffusion. The exchange and persistence times as defined in Sec. III D are shown in Fig. 8(c). Several changes in dynamics are evident, providing one persistence time (time to first change of dynamics), three exchange times, and one lower bound on exchange time (time between final change in dynamics and end of trajectory).

Molecules that display temporal heterogeneity as assessed by the sliding window approach are not rare in the data sets examined here. 31 of 195 assessed molecules are temporally heterogeneous. Given that the method used here for identifying temporal heterogeneity is tuned to exclude false positives and is only sensitive to some changes of dynamics, there may be additional heterogeneous molecules that are not identified as such. Despite the relative abundance of temporally heterogeneous molecules identified, molecules that display the full breadth of heterogeneity demonstrated across all probed molecules (nearly three orders of magnitude) are not commonly observed. Instead, molecules such as that shown in Fig. 8 are typical, with regimes of typical
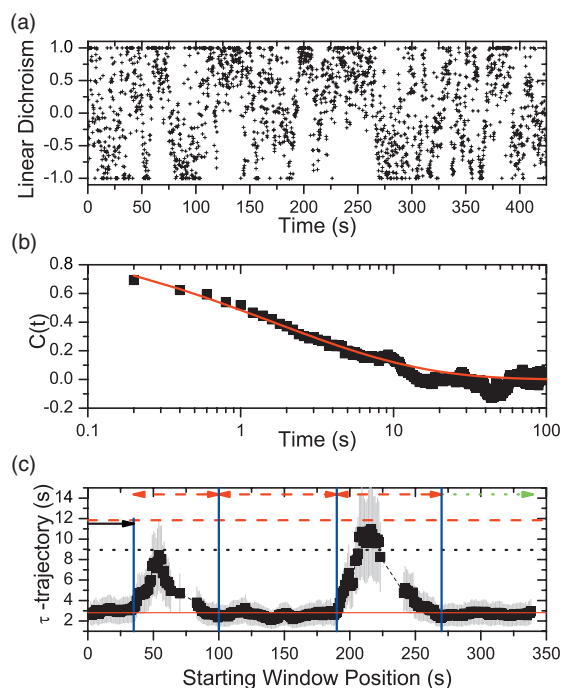
FIG. 8. Data from a representative heterogeneous molecule. (a) LD and (b) ACF. Standard error on the points of the ACF is smaller than symbol size and therefore not shown. Stretched exponential fit to the ACF yields with τ_c=4.4 s. (c) τ-trajectory for this molecule. The error bars indicate the standard deviation of 41% associated with a high sampling rate trajectory and window width of $20\tau_c$ using linear fits as shown in Fig. 4(a), open green triangles. Solid red line is $\tau_{traj,med}$=2.81 s. Dashed red line indicates the value below which 95% of the points within τ-trajectory fall ($3.4\tau_{traj,med}$ =9.5 s). Dotted black line indicates lowest position at which 95% of the points within τ trajectory would fall for a molecule satisfying this criterion for temporal heterogeneity ($2.41\tau_{traj,med}$=6.8 s). Because the red dashed line is above the black dotted line, this molecule is designated temporally heterogeneous. Persistence time (black solid arrow), exchange times (red dashed arrows), and lower bound on exchange time (green dotted arrow) are indicated.

behavior (low sampling rate, fast rotations) and regimes 3–5 times slower. In the data collected, the largest difference between fast and slow relaxation times seen in any particular molecule's trajectory is just over an order of magnitude. Failure to find molecules displaying more substantial changes in dynamics is to a certain extent set by the method of analysis as described in Sec. III D. However, molecules in which a portion of the trajectory shows very slow dynamics should be identifiable via visual inspection of the LD trajectory. Of the 279 features whose LDs were examined, three molecules appear to undergo significant changes in dynamics that are not reported by the sliding window process. Two of these molecules are not otherwise categorized, as their ACFs are not well fit with stretched exponential or linear fits. The other such molecule is categorized as a typical, homogeneous molecule as the molecule exits a very slow environment and transitions into a fast one shortly after the experiment begins. Figure 9 shows the LDs of each of these molecules.

While the multiple rotational time constants displayed by molecules depicted in Fig. 9 have not been quantified, it can be appreciated that these molecules are exhibiting more drastic changes in their dynamics than those the sliding window procedure identifies as heterogeneous. In the full data set described in this manuscript, 26 of 241 molecules have
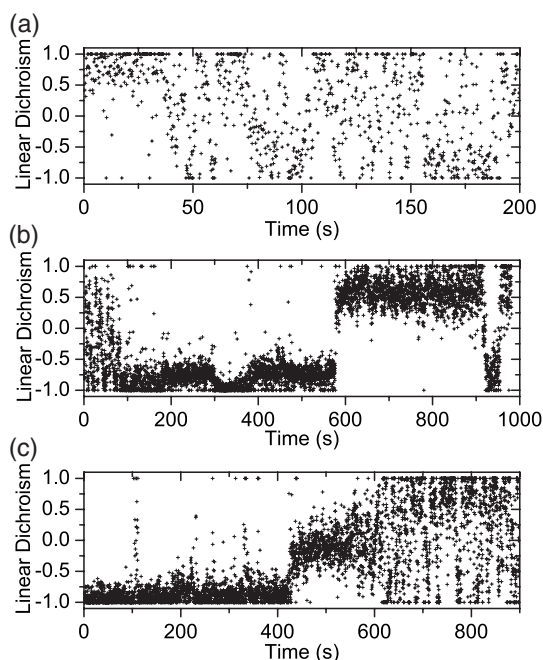

FIG. 9. LD from the three molecules in the data set exhibiting larger changes in dynamics than can be quantified using the sliding window technique. (a) Molecule that shows no rotation for first ~40 s of trajectory followed by consistent fast rotations over the remaining 450 s of the trajectory. Only the first 200 s of the trajectory is shown to highlight early portion. (b) Molecule exhibiting rapid rotations for ~70 s, followed by transition into an environment in which only librations occur, followed by a large angular jump and continued librations, before a return to more typical behavior at ~920 s. (c) Molecule librating for ~420 s, showing slow rotation for ~150 s, before transitioning into an environment with typical rotations.

time constants at least an order of magnitude longer than the median relaxation time of the data set (1.7 s). As such, it might be expected that of molecules undergoing exchange, molecules rotating with a time constant near the median during a portion of the trajectory would exhibit an exchange into an environment characterized by dynamics at least an order of magnitude slower ~10% of the time. Indeed, three molecules of this type are identified compared to 31 molecules with heterogeneous dynamics in which smaller dynamical changes are seen. This suggests that within the mosaic of local environments, exchange is as likely to occur between dynamically disparate environments as between dynamically similar environments. This conclusion differs from the findings of Zondervan *et al.*,[25] which suggest that there is a population of very slow molecules that does not interchange with molecules in faster environments. Our finding also strongly suggests that the probe molecule employed in this study is not so large or massive as to either average over spatially heterogeneous dynamics in the system or to set up nonrepresentative environments locally around the probe molecules.[48–51]

While the molecule depicted in Fig. 8 demonstrates several dynamic exchanges, all molecules classified as dynamically heterogeneous demonstrate at least a persistence time [time to first detected exchange, black solid arrow in Fig. 8(c)] and a lower bound on exchange time [time from final detected exchange until photobleaching, green dotted arrow in Fig. 8(c)]. Molecules experiencing more than one change
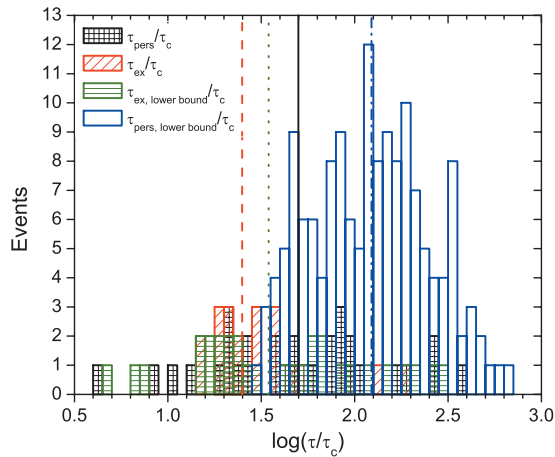
FIG. 10. Histograms of τ_{pers}/τ_c (black bars with checks), τ_{ex}/τ_c (red bars with diagonal lines), $\tau_{ex,lower\ bound}/\tau_c$ (olive bars with horizontal lines), and $\tau_{pers,lower\ bound}/\tau_c$ (blue bars) as compiled from the 195 molecules assessed for temporal heterogeneity and found to be heterogeneous (τ_{pers}/τ_c, τ_{ex}/τ_c and $\tau_{ex,lower\ bound}/\tau_c$) or homogeneous ($\tau_{pers,lower\ bound}/\tau_c$). Lines indicate median values: $\tau_{pers}/\tau_c = 50$ (black solid line), $\tau_{ex}/\tau_c = 25$ (red dashed line), $\tau_{ex,lower\ bound}/\tau_c = 35$ (olive dotted line), and $\tau_{pers,lower\ bound}/\tau_c = 123$ (blue dash-dot line).

of dynamics during the experiment additionally report at least one exchange time [time between detected exchanges, red dashed arrows in Fig. 8(c)]. Molecules that are assessed for heterogeneity and deemed homogeneous display a lower bound on persistence time set by the lifetime of the molecule. Histograms of these four time scales for the 195 molecules assessed for temporal heterogeneity are shown in Fig. 10. The median ratio of the molecules' lower bound on persistence times relative to their rotational correlation times ($\tau_{pers,lower\ bound}/\tau_c = 123$) is significantly longer than the that of persistence times relative to rotational correlation times measured on molecules that experience exchange ($\tau_{pers}/\tau_c = 50$). This suggests that, as predicted by KCM, molecules exhibiting changes in dynamics during a particular time are more likely to undergo repeated changes in dynamics; i.e., such molecules are in a space-time region in which dynamic exchange is common.[47] Comparing exchange and lower bound on exchange times is also consistent with this finding. Both times can only be measured from molecules deemed heterogeneous, and thus these times would be expected to be similar to or (for lower bound on exchange time) shorter than persistence times. The median values of exchange and lower bound on exchange values relative to rotational relaxation times of those molecules are $\tau_{ex}/\tau_c = 25$ and $\tau_{ex,lower\ bound}/\tau_c = 35$. The range of τ_{ex}/τ_c detected was 15–200. The median rotational correlation time of the rubrene probe (1.7 s) is approximately an order of magnitude larger than the alpha relaxation of glycerol at this temperature (0.21 s).[52] As such, we expect that our method is sensitive to τ_{ex}/τ_α in the range of ~100–5000; even in the absence of a sliding window, the lower bound on measured τ_{ex}/τ_α would be ~10, as set by the size of the probe relative to a glycerol molecule. The actual range of τ_{ex}/τ_α measured was 120–1600, with a median $\tau_{ex}/\tau_\alpha = 202$. As pointed out in Sec. III D, exchange time as measured by subensemble experiments performed previously is more akin to persistence time.

Additionally, the time Orrit refers to as exchange time is akin to lower bound on persistence time. Measurements described here show $\tau_{pers}/\tau_\alpha = 405$ and $\tau_{pers,lower\ bound}/\tau_\alpha = 996$. These ratios are larger than those found from subensemble experiments on OTP but significantly smaller than the value measured via SM experiments on glycerol, which in the terminology presented here is $\tau_{pers,lower\ bound}/\tau_\alpha = 10^6$. While the origin of these discrepancies remains to be fully elucidated, the data and analysis methods presented here provide a framework and best practice techniques for assessing the breadth of spatial and existence of temporal heterogeneity over select time scales in supercooled liquids via SM microscopy.

IV. CONCLUSION

We have demonstrated that WF illumination epifluorescence SM microscopy, which allows for parallel data collection, has manifestations in measured intensity and linear dichroism. Even in the presence of realistic noise, however, these effects do not alter expected exponentiality of ACFs for molecules exhibiting homogeneous rotational diffusion. On the other hand, typical experimental trajectories are short enough such that accuracy of measured relaxation time and stretching exponent are diminished. The spread of stretching exponents expected in the presence of homogeneous rotational diffusion for trajectories of typical length eliminates the possibility of identifying temporal heterogeneity from the value of the stretching exponent. Additionally, to maximize accuracy in reported relaxation times, trajectory-dependent fitting taking into account both trajectory length and sampling rate is performed. Stretched exponential fits provide the most accurate relaxation times for trajectories collected at low sampling rate, while at high sampling rate, stretched exponential fits are most accurate for long trajectories and linear fits to the early part of the ACF are best for short trajectories. Trajectory-dependent fitting avoids unintentional subensemble selection. A technique with which to identify changes in the rotational dynamics of a SM independent of the best fit stretching exponent to the full trajectory is introduced. A sliding window of autocorrelations leads to a set of relaxation times termed as τ-trajectory, which allows for both identification of temporally heterogeneous molecules as well as their persistence and exchange times within experimentally and analysis-defined bounds.

The experimental data presented here show that rubrene in glycerol at $T_g + 14$ K exhibits significant spatial heterogeneity, with a spread of relaxation times of nearly three orders of magnitude, quite similar to that measured previously via SM microscopy in glycerol.[25] On the contrary, while that study found no temporally heterogeneous molecules, the current study finds ~15% of the assessable molecules display distinct changes in their dynamics over the course of the experiment that can be detected with the technique described here. Among these molecules, $\tau_{ex}/\tau_\alpha = 202$ and $\tau_{pers}/\tau_\alpha = 405$. Additionally, the presence of several molecules exhibiting greater changes in dynamics than can be quantitatively assessed suggests that exchange between dynamically disparate environments occurs in the proportion expected given the

number of very slow molecules present. Continued optimization of SM experiments and analysis thereof should allow sensitivity to a broader range of dynamic exchanges. Additional experiments will also reveal the temperature dependence of the proportion of molecules experiencing exchange in the detectable range. Both additions will help clarify the picture of supercooled liquids as a complex mosaic of local environments.

ACKNOWLEDGMENT

[1] H. Sillescu, J. Non-Cryst. Solids **243**, 81 (1999).
[2] X. Y. Xia and P. G. Wolynes, Proc. Natl. Acad. Sci. U.S.A. **97**, 2990 (2000).
[3] M. T. Cicerone, F. R. Blackburn, and M. D. Ediger, J. Chem. Phys. **102**, 471 (1995).
[4] C. Y. Wang and M. D. Ediger, J. Phys. Chem. B **103**, 4177 (1999).
[5] M. T. Cicerone and M. D. Ediger, J. Phys. Chem. **97**, 10489 (1993).
[6] T. Inoue, M. T. Cicerone, and M. D. Ediger, Macromolecules **28**, 3425 (1995).
[7] P. L. Kuhns and M. S. Conradi, J. Chem. Phys. **77**, 1771 (1982).
[8] X. H. Qiu and M. D. Ediger, J. Phys. Chem. B **107**, 459 (2003).
[9] S. A. Reinsberg, X. H. Qiu, M. Wilhelm, H. W. Spiess, and M. D. Ediger, J. Chem. Phys. **114**, 7299 (2001).
[10] U. Tracht, M. Wilhelm, A. Heuer, H. Feng, K. Schmidt-Rohr, and H. W. Spiess, Phys. Rev. Lett. **81**, 2727 (1998).
[11] R. Böhmer, G. Hinze, G. Diezemann, B. Geil, and H. Sillescu, Europhys. Lett. **36**, 55 (1996).
[12] B. Schiener, R. V. Chamberlin, G. Diezemann, and R. Bohmer, J. Chem. Phys. **107**, 7746 (1997).
[13] B. Schiener, R. Bohmer, A. Loidl, and R. V. Chamberlin, Science **274**, 752 (1996).
[14] S. A. Hutcheson and G. B. McKenna, J. Chem. Phys. **129**, 074502 (2008).
[15] K. Schröter and E. Donth, J. Chem. Phys. **113**, 9101 (2000).
[16] R. Zondervan, T. Xia, H. van der Meer, C. Storm, F. Kulzer, W. van Saarloos, and M. Orrit, Proc. Natl. Acad. Sci. U.S.A. **105**, 4993 (2008).
[17] D. W. Davidson and R. H. Cole, J. Chem. Phys. **19**, 1484 (1951).
[18] P. Lunkenheimer, A. Pimenov, B. Schiener, R. Bohmer, and A. Loidl, Europhys. Lett. **33**, 611 (1996).
[19] N. Menon, K. P. Obrien, P. K. Dixon, L. Wu, S. R. Nagel, B. D. Williams, and J. P. Carini, J. Non-Cryst. Solids **141**, 61 (1992).
[20] L. A. Deschenes and D. A. V. Bout, J. Phys. Chem. B **106**, 11438 (2002).
[21] A. Schob, F. Cichos, J. Schuster, and C. von Borczyskowski, Eur. Polym. J. **40**, 1019 (2004).
[22] A. N. Adhikari, N. A. Capurso, and D. Bingemann, J. Chem. Phys. **127**, 114508 (2007).
[23] R. A. L. Vallée, T. Rohand, N. Boens, W. Dehaen, G. Hinze, and T. Basche, J. Chem. Phys. **128**, 154515 (2008).
[24] C. Y. J. Wei and D. A. V. Bout, J. Phys. Chem. B **113**, 2253 (2009).
[25] R. Zondervan, F. Kulzer, G. C. G. Berkhout, and M. Orrit, Proc. Natl. Acad. Sci. U.S.A. **104**, 12628 (2007).
[26] H. Uji-i, S. M. Melnikov, A. Deres, G. Bergamini, F. De Schryver, A. Herrmann, K. Mullen, J. Enderlein, and J. Hofkens, Polymer **47**, 2511 (2006).
[27] R. Vallée, M. Cotlet, J. Hotkens, and F. De Schryver, Macromolecules **36**, 7752 (2003).
[28] M. T. Cicerone and M. D. Ediger, J. Chem. Phys. **103**, 5684 (1995).
[29] T. K. Herman, S. A. Mackowiak, and L. J. Kaufman, Rev. Sci. Instrum. **80**, 016107 (2009).
[30] R. Chance, A. Prock, and R. Silbey, Adv. Chem. Phys. **37**, 1 (1978).
[31] J. H. Robertson, J. Sci. Instrum. **40**, 506 (1963).
[32] J. B. Segur and H. E. Oberstar, Ind. Eng. Chem. **43**, 2117 (1951).
[33] J. C. Crocker and D. G. Grier, J. Colloid Interface Sci. **179**, 298 (1996).
[34] cow.physics.wisc.edu/~craigm/idl/math.html
[35] C. Y. J. Wei, Y. H. Kim, R. K. Darst, P. J. Rossky, and D. A. Vanden Bout, Phys. Rev. Lett. **95**, 173001 (2005).
[36] P. M. Wallace, D. R. B. Sluss, L. R. Dalton, B. H. Robinson, and P. J. Reid, J. Phys. Chem. B **110**, 75 (2006).
[37] M. D. Ediger, Annu. Rev. Phys. Chem. **51**, 99 (2000).
[38] P. G. Debenedetti and F. H. Stillinger, Nature (London) **410**, 259 (2001).
[39] C. Y. Lu and D. A. Vanden Bout, J. Chem. Phys. **125**, 124701 (2006).
[40] C. Y. Lu and D. A. V. Bout, J. Chem. Phys. **128**, 10 (2008).
[41] D. Bingemann, Chem. Phys. Lett. **433**, 234 (2006).
[42] J. T. Fourkas, Opt. Lett. **26**, 211 (2001).
[43] M. S. Robbins and B. J. Hadwen, IEEE Trans. Electron Devices **50**, 1227 (2003).
[44] G. Hinze, G. Diezemann, and T. Basche, Phys. Rev. Lett. **93**, 203001 (2004).
[45] C. Y. J. Wei, C. Y. Lu, Y. H. Kim, and D. A. V. Bout, J. Fluoresc. **17**, 797 (2007).
[46] H. Yang, J. Chem. Phys. **129**, 074701 (2008).
[47] Y. Jung, J. P. Garrahan, and D. Chandler, J. Chem. Phys. **123**, 084509 (2005).
[48] L. Wang and R. Richert, J. Chem. Phys. **120**, 11082 (2004).
[49] M. Yang and R. Richert, Chem. Phys. **284**, 103 (2002).
[50] C. Y. Wang and M. D. Ediger, J. Chem. Phys. **112**, 6933 (2000).
[51] R. Zangi, S. A. Mackowiak, and L. J. Kaufman, J. Chem. Phys. **126**, 104501 (2007).
[52] P. Lunkenheimer, U. Schneider, R. Brand, and A. Loidl, Contemp. Phys. **41**, 15 (2000).